Assessment of dynamic structural instabilities across 24 cubic inorganic halide perovskites

Ruo Xi Yang,[1,2] Jonathan M. Skelton,[3] Estelina L. da Silva,[4] Jarvist M. Frost,[5] and Aron Walsh[1,6,a]

[1]*Department of Materials, Imperial College London, Exhibition Road, London SW7 2AZ, UK*

[2]*Molecular Foundry, Lawrence Berkeley National Laboratory, 1 Cyclotron Rd, Berkeley, CA 94720, USA*

[3]*Department of Chemistry, University of Manchester, Manchester M13 9PL, UK*

[4]*Instituto de Diseño para la Fabricación y Producción Automatizada, MALTA Consolider Team, Universitat Politècnica de València, València, Spain, 46022 Valencia, Spain*

[5]*Department of Physics, Imperial College London, Exhibition Road, London SW7 2AZ, UK*

[6]*Department of Materials Science and Engineering, Yonsei University, Seoul 120-749, Korea*

(Dated: 20 November 2020)

Metal halide perovskites are promising candidates for next-generation photovoltaic and optoelectronic applications. The flexible nature of the octahedral network introduces complexity when understanding their physical behavior. It has been shown that these materials are prone to decomposition, phase competition, and the local crystal structure often deviates from the average space group symmetry. To make stable phase-pure perovskites, understanding their structure–composition relations is of central importance. We demonstrate, from lattice dynamics calculations, that the 24 inorganic perovskites ABX_3 (A = Cs, Rb; B = Ge, Sn, Pb; X = F, Cl, Br, I) exhibit instabilities in their cubic phase. These instabilities include cation displacements, octahedral tilting, and Jahn-Teller distortions. The magnitudes of the instabilities vary depending on the chemical identity and ionic radii of the composition. The tilting instabilities are energetically dominant, and reduce as the tolerance factor increases, whereas cation displacements and Jahn-Teller type distortions depend on the interactions between the constituent ions. We further considered representative tetragonal, orthorhombic and monoclinic perovskites phases to obtain phonon-stable phases for each composition. This work provides insights into the thermodynamic driving force of the instabilities and will help guide synthesis in material screening.

I. INTRODUCTION

Since the discovery of photoconductivity in the caesium lead halides ($CsPbX_3$ [X = Cl, Br, I])[1], the semiconducting properties of halide perovskites have attracted significant research attention, including analogous compounds based on Sn and Ge.[2–4] Interest has since expanded to the hybrid organic-inorganic perovskites with potential applications including field-effect transistors,[5] photovoltaics,[6,7] and light-emitting diodes.[8] This family of materials display a unique combination of physical and chemical properties, including fast ion and electron transport,[9–11] long carrier diffusion lengths,[12] and high quantum efficiency.[13]

The crystallography of lead halide perovskites dates back to the 1950s, where the high-temperature crystal structures of the $CsPbX_3$ series were determined to be the archetypal cubic perovskite structure (space group $Pm\bar{3}m$). The same structure was later reported for the $CH_3NH_3PbX_3$ series.[14] In all cases, phase transitions to lower symmetry perovskite phases are observed as the temperature is reduced, e.g. in $CsPbCl_3$ there is a tran-

sition to a tetragonal phase at 320 K, an othorhombic phase at 316 K, and a monoclinic phase at 310 K.[15]

The nature of the high temperature cubic phase of the halide perovskites has received less attention. Analysis of the X-ray pair distribution functions of $CH_3NH_3SnBr_3$ suggested that the the local cubic symmetry was broken with significant distortions of the corner-sharing octahedral network.[16] It was recently confirmed, from both inelastic X-ray and neutron total scattering that the cubic phase of $CH_3NH_3PbI_3$ is also symmetry broken.[17–19] These observations have been associated with rotational disorder of the molecular $CH_3NH_3^+$ cation.

Relatively little work has been reported on the inorganic halide perovskite counterparts. It was shown by X-ray total scattering that $CsPbX_3$ nanocrystals always exhibit orthorhombic tilting of the octahedra within locally-ordered subdomains.[20] Furthermore, low-frequency Raman scattering has confirmed that $CsPbBr_3$ undergoes dynamical polar fluctuations at 300 K, even though analysis of XRD measurement suggests the structure to be cubic at that temperature.[21] Evidence of symmetry breaking has also been reported from analysis of the temperature-dependant photoluminescence of Cs and CH_3NH_3 compounds.[22]

In this work, we demonstrate that vibrational instabilities are common to inorganic halide perovskites in the

[a]Electronic mail: a.walsh@imperial.ac.uk

ABX$_3$ (A = Cs, Rb; B = Ge, Sn, Pb; X = F, Cl, Br, I) family. The associated dynamic disorder is a consequence of the flexibility associated with the corner-sharing network of inorganic octahedra, which includes rigid-unit tilting modes, distortions of the octahedra, and cation displacements. Through first-principles lattice-dynamics calculations, we assess the chemical and thermodynamic driving forces for these instabilities and discuss the consequences for the material properties.

II. CLASSIFICATION OF STRUCTURAL INSTABILITIES

The aristotype cubic perovskite structure is usually adopted at high temperature, while at low temperature an assortment of lower symmetry phases (e.g. tetragonal, orthorhombic, monoclinic, rhombohedral) are observed. The lattice distortions associated with these transitions can be divided into three categories: (i) polar displacement of the A or B cations away from their high symmetry positions; (ii) rigid tilting of the corner-sharing BX$_6$ octahedra; and (iii) collective Jahn-Teller distortion of the BX$_6$ octahedra.[23–26]

Cation displacements are usually responsible for so-called proper ferroelectricity, which is associated with the presence of a soft polar phonon mode at the Γ point in the phonon Brillouin Zone. For example, BaTiO$_3$ and PbTiO$_3$ exhibit spontaneous polarization due to the displacement of the Ti atom from the center of its octahedron.[27] The displacive phonon mode is at the Brillouin Zone center which implies an in-phase periodic distortion across the crystal and thus a macroscopic polarization.

On the other hand, octahedral tilting due to zone-boundary phonon modes (e.g. at the M $(\frac{1}{2}, \frac{1}{2}, 0)$ or R $(\frac{1}{2}, \frac{1}{2}, \frac{1}{2})$ special points in the first Brillouin Zone of the cubic structure) result in an anti-phase periodic distortion. The opposite polarization generated in neighbouring unit cells cancels out and there is no resulting macroscopic polarization. Due to this, these are often referred to as antiferroelectric or antipolar distortions. In-phase tilting corresponds to an M_3^+ mode denoted by + in Glazer's notation $a^0a^0c^+$, whereas out-of-phase tilting corresponds to an R_4^+ mode denoted by a − sign in $a^0a^0c^-$.[28] A linear combination of both modes can define all the possible rigid tilting modes in the perovskite systems.[24] We previously explored the behaviour of the M_3^+ mode in the caesium lead and tin halides.[29]

A third type of distortion is due to the Jahn-Teller (JT) effect. The octahedra distort by elongation or shortening of the B-X bond, and sometimes by off-centering of the B cation. A first-order JT distortion is commonly observed in transition metals with degenerate electronic ground states such as Cu(II). Shortening/elongating the nearest-neighbor bonds and generating a crystal field lifts the degeneracy of the partially occupied d band (e.g. d^9 for Cu $^{2+}$ in KCuF$_3$) and allows for a lowering of the en-

ergy. Cases such as Pb(II) 6s^2 where the structural distortion allows mixing with nominally empty 6s^0 orbitals are usually referred to as second-order JT distortions.[30]

These classes of distortion are not necessarily independent, but can couple via (anharmonic) interactons between phonon modes. Benedek et $al.$ found that this coupling acts to suppress ferroelectricity in many oxide perovskites.[25] Moreover, there has been large interest in designing new "hybrid improper" ferroelectricity through coupling between non-polar modes in Ruddlesden-Popper phase perovskites.[31] In particular, tilting coupled with Jahn-Teller distortions (so-called "pseudo" rotations) are considered one route for designing multiferroic materials.[32–34]

III. METHODS

Model structures for 24 inorganic halide compounds ABX$_3$ (A = Cs, Rb; B = Ge, Sn, Pb; X = F, Cl, Br, I) were taken from the Inorganic Crystal Structure Database where available, and the remaining generated by atomic substitution of similar structures. Density functional theory (DFT) as implemented in the pseudopotential plane-wave code VASP[35,36] was used to optimize the crystal structures of four commonly-observed phases $viz.$ cubic $Pm\bar{3}m$, tetragonal $P4/mmm$, orthorhombic $Pnma$ and monoclinic $P2_1/m$. The structures were fully relaxed with the PBEsol exchange-correlation functional.[37–39] Explicit convergence testing identified a plane-wave kinetic-energy cutoff of 800 eV and an electronic Brillouin zone sampling with an 8×8×8 mesh for the cubic and orthorhombic phases, a k-point mesh of 6×6×8 mesh for the tetragonal phases, and a 4×4×4 mesh monoclinic phases to produce accurate phonon frequencies.

The formation enthalpy of each crystal can be calculated from

$$\Delta H_{ABX_3} = E_{ABX_3} - \mu_A - \mu_B - 3\mu_X \quad (1)$$

where E_{ABX_3} is the total energy obtained in DFT calculation, μ are the chemical potentials of the constituent elements. When comparing the differences in ΔH_{ABX_3} between different phases with the same composition, the μ terms cancel and ΔH is simply the difference in DFT total energies for the different phases.

Harmonic phonon dispersion and density of states (DoS) curves were obtained using the finite displacement method implemented in the open-source PHONOPY package, with VASP used as the force calculator. For each phase, a series of symmetry-independent displacements were generated in 2×2×2 supercell expansions, chosen to be commensurate with the zone-boundary symmetry points, to obtain the force–constant matrices, which were then used to obtain phonon frequencies and eigenvectors at arbitrary phonon wavevectors q.

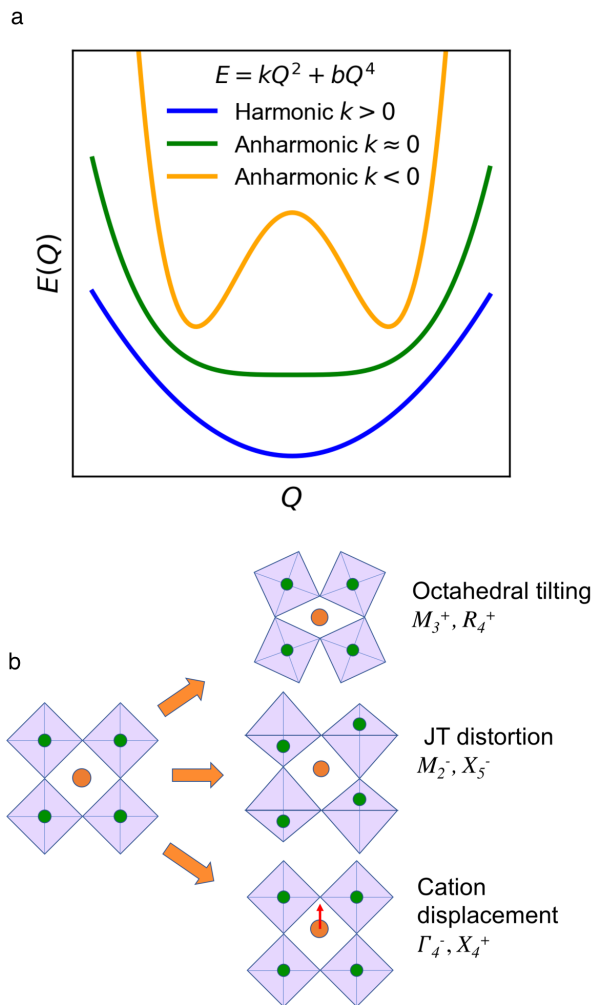To map out the anharmonic potential energy surfaces associated with the phonon instabilities, we use the open-

FIG. 1. a) Schematic potential energy surface along harmonic and anharmonic phonon modes as a function of the phonon normal mode coordinate Q. b) Schematic illustration of the three classes of distortion observed in cubic perovskites and the associated irreducible representations from group theory. The ferroelectric displacement is associated with a zone-centre phonon mode that leads to macroscopic electric polarization. The octahedral tilting is associated with a zone-boundary phonon mode and results in an expansion of the unit cell. Jahn-Teller distortions can be associated with either a zone-centre or zone-boundary mode, but in the cubic perovskites studied here manifest as zone-boundary M or X modes. These distortions may coexist in real materials.

source MODEMAP package.[40,41] A sequence of displaced structures in a commensurate supercell expansion are generated by displacing along the phonon eigenvectors over a range of amplitudes of the normal-mode coordinate Q, and the total energies of the "frozen phonon" structures are evaluated from single-point DFT calculations. The $E(Q)$ curves are then fitted to a polynomial function, with the number of terms depending on the form of the potential well. These anharmonic energy surfaces then effectively include higher-order terms in the

potential energy as a function of the nuclear coordinates, in the basis of the harmonic eigenvectors.

IV. PHASE DIVERSITY OF INORGANIC HALIDE PEROVSKITES

A search of the literature shows that only a fraction of the 24 chemical combinations studied here have been reported experimentally, as summarised in Table I. The majority of the inorganic halide perovskites are reported to adopt the cubic structure (space group $Pm\bar{3}m$) at high temperature, including $CsGeCl_3$, $CsPbCl_3$, $CsPbBr_3$, $CsPbI_3$, $CsSnI_3$, $RbGeI_3$, $RbPbF_3$,[42–48] while $CsSnBr_3$ has been reported to be cubic at room temperature.[2]

The phase diversity can be qualitatively explained using the concept of the tolerance factor α introduced by Goldschmidt[49] where:

$$\alpha = (r_A + r_X)/\sqrt{2}(r_B + r_X) \qquad (2)$$

Values of $\alpha < 1$ are usually associated with octahedral tilting due to an A cation that is smaller than the ideal value for the BX_3 octahedral framework. This is the case for the majority of compounds considered here (see Table I), which explains the most stable phases being lower-symmetry space groups, typically $Pnma$, which is the ground state structure of $CsPbCl_3$, $CsSnI_3$, $RbPbF_3$, $RbPbI_3$.[43,45,46,48]

However, many of the Ge compounds have $\alpha > 1$, which often leads to B-site displacements and hence to polar structures due to loss of centrosymmetry. For instance, $CsGeCl_3$, $CsGeBr_3$ and $CsGeI_3$ are reported to undergo an order-disorder phase transition from cubic to rhombehedral ($R3m$) under ambient conditions.[4,50]

We computed the formation enthalpy and phonon dispersion of four phases for each composition (see Supporting Information). Imaginary frequencies (soft modes) present in the phonon dispersion indicate dynamic instabilities at 0 K, whereas the absence of imaginary modes indicates the structure is a local potential-energy minimum. The stable phases of each composition are summarised in Table I. None are found to be most stable in the cubic or tetragonal phases, with the corresponding dispersion curves showing soft modes across the whole Brillouin zone, indicating multiple dynamical instabilities. Similarly, the tetragonal phases, derived from the cubic structure by in-phase octahedral rotation with Glazer notation $a^0a^0c^+$, also show multiple instabilities. This indicates that the tetragonal phases are intermediates formed on the symmetry lowering path from cubic to the lowest-energy symmetry-broken ground state.

The lower-symmetry phases of all compositions have more favourable formation enthalpies than the cubic phase, and the orthorhombic $Pnma$ and monoclinic $P2_1/m$ phase also have lower formation energies than tetragonal $P4/mmm$ structure, showing that additional distortions lower the energy (Table I). This shows that

the tetragonal phases are both dynamically and energetically unstable at 0 K. However, the formation enthalpies of the $Pnma$ and $P2_1/m$ phases are similar, implying that the energy gain for further lowering the symmetry from orthorhombic to monoclinic is small. Consideration of the formation enthalpy differences can help to explain why the orthorhombic phase is the most commonly observed for halide perovskites.

V. HARMONIC PHONON INSTABILITIES

In the cubic perovskite phase, all compounds were found to exhibit imaginary modes at certain symmetry points in the phonon Brillouin zone (Table II). All compounds exhibit M-point instabilities. Apart from CsSnBr$_3$, all the compounds also exhibit Γ-point instabilities. Perovskites other than CsPbF$_3$, CsSnBr$_3$ and CsSnCl$_3$ also show X-point instabilities. In addition, R-point instabilities are found in all perovskites other than CsGeX$_3$ (X = F, Cl, Br) and CsSnF$_3$. It is worth noting that all the Rb compounds feature instabilities at every high-symmetry point in the cubic perovskite Brillouin zone, in agreement with the fact that fewer Rb halide perovskites have been identified experimentally.

To provide a better understanding of the underlying chemical driving forces, we have categorized the instabilities into zone-centre cation displacements, zone-boundary octahedral tilting, and Jahn-Teller distortions (Fig. 1). We will show in the following sections how the chemistry of the compound determines the types of instabilities that occur.

A. Octahedral tilting

Instabilities corresponding to the octahedral tilting can be found at both the M and R points. Among the 24 cubic halide perovksites all show M-point instabilities, allowing comparisons to be made between the systems. Although the imaginary modes occur at the same reciprocal-space wavevector, they can correspond to different types of distortions in real space. The harmonic eigenvectors associated with these modes were therefore inspected to determine the distortion type. Some compounds have more than one M-point instability, but for simplicity we confine our discussion to the "most" imaginary phonon branch, i.e. the one lying lowest in the phonon dispersion, which is indicative of the largest negative curvature of the potential-energy surface around $Q = 0$.

CsSnCl$_3$, CsSnBr$_3$, CsSnI$_3$, CsPbX$_3$, RbGeBr$_3$, RbGeI$_3$, RbSnCl$_3$, RbSnBr$_3$, RbSnI$_3$ and RbPbX$_3$ display M_3^+ instabilities corresponding to an in-phase octahedral tilting with Glazer notation $a^0a^0c^+$ (Fig. 3). For CsGeX$_3$, CsSnF$_3$, RbGeF$_3$, RbGeCl$_3$, RbSnF$_3$, the lowest-lying phonon mode corresponds to the M_2^- mode,

which corresponds to a Jahn-Teller distortion and will be discussed in the following section.

Using the eigenvectors associated with the M_3^+ mode, we mapped out the potential energy surface E as a function of the normal-mode coordinate Q. The $E-Q$ curves for M_3^+ in all compositions that adopt this instability are shown in Fig. 2. The resulting $E-Q$ surfaces correspond to symmetrical double-well potentials, with the central point $Q = 0$ being the reference cubic phase. The well depth indicates the enthalpy gained by breaking the crystal symmetry. Shallow well depths ($\Delta E \approx k_B T$) suggest that thermal energy can allow the system to explore parts of the potential close to $Q = 0$. Such anharmonic double wells are common in perovskite structures[59,60] and are characteristic of ferroelectric transitions for cases where Q represents a polar distortion.[61,62]

The Rb compounds possess deeper minima than their Cs counterparts (Fig. 2), indicating a stronger energetic driving force for tilting. Within the Rb or Cs series, there are two distinct trends: (i) the double well depth increases monotonically when the B-site cation goes from Ge $\rightarrow$ Sn $\rightarrow$ Pb; (ii) for compounds with the same B-site cation, the well depth increases as the X site is substituted from F $\rightarrow$ Cl $\rightarrow$ Br $\rightarrow$ I.

Both phenomena can be interpreted by the geometry of the cubic perovskite crystal. Firstly, the Rb cation is too small for the octahedral cavity, which drives the collapse of the network towards the A cation. Secondly, the interplay between the size of the A-site cation and the volume of the cage also determines the magnitude of the tilting instability, i.e. the larger the ratio of the size of the cavity to the A-site cation, the stronger the tilting. This again follows the tolerance factor α. If α is too small, the octahedral network will tend to tilt, as observed in RbPbX$_3$, which have the smallest α (0.82 – 0.86) and the largest well depths. On the other hand, when α is close to or greater than one, such as in CsGeX$_3$ (0.98–1.11), RbGeF$_3$ (1.05) and RbGeCl$_3$ (0.98), the M_3^+ tilting instability is not seen due to the limited space in the cuboctahedral cavity.

An almost-identical trend is observed for the out-of-phase tilting R_4^+ mode, which suggests that the behavior is not limited to in-phase tilting but is common to all tilting modes.

B. Zone-boundary Jahn-Teller distortion

In addition to rigid octahedral tilting, some compounds show M-point imaginary frequencies associated with a different type of distortion. For most of the Ge perovskites and some of the Sn perovskites, including CsGeF$_3$, CsGeCl$_3$, CsGeBr$_3$, CsGeI$_3$, RbGeF$_3$, RbGeCl$_3$, CsSnF$_3$, and RbSnF$_3$, the imaginary modes with the steepest local curvature correspond to an M_2^- instability (Fig. 4). Instead of rigid rotation of the octahedra with fixed bond lengths, the B–X bonds either shorten or lengthen and the B-site cation is displaced

TABLE I. Difference in formation enthalpy (ΔH) for tetragonal ($P4/mbm$, $a^0a^0c^+$), orthorhombic ($Pnma$, $a^+b^-b^-$) and monoclinic ($P2_1/m$, $a^+b^-c^-$) phases of the ABX$_3$ perovskites with respect to the cubic phase ($Pm\bar{3}m$, $a^0a^0a^0$). Phases identified as being phonon stable and experimentally-observed structures are also given. The tolerance factor is calculated using the Shannon ionic radii where available[51], while the radius for Sn(II) (1.15 Å) is taken from Ref. 52.

| Composition	ΔH (meV/formula)			Phonon stable phase	Experimentally observed	Tolerance factor
	$P4/mbm$	$Pnma$	$P2_1/m$			
CsGeF$_3$	-0.9	-1	-0.7			1.11
CsGeCl$_3$	-0.3	-1	-0.3		$Pm\bar{3}m$ at 449 K/ $R3m$ at RT[53]	1.02
CsGeBr$_3$	-2.6	-4.0	-1.1		$R3m$ at RT[4]	1.01
CsGeI$_3$	-2.6	-4.4	-0.2		$R3m$ at RT[4]	0.98
CsSnF$_3$	0.2	-1.8	-2.5			0.92
CsSnCl$_3$	-0.9	-27.7	-27.3		$Pm\bar{3}m$ at RT[54]	0.88
CsSnBr$_3$	-22.8	-35.9	-35	$Pnma$ and $P2_1/m$	$Pm\bar{3}m$ at RT, $Pnma$ at 100 K[2,55]	0.87
CsSnI$_3$	-634.1	-692.9	-691.8	$P2_1/m$	$Pm\bar{3}m$ at 500 K; $Pnma$ at RT[46]	0.86
CsPbF$_3$	-20.4	-32	-32	$Pnma$ and $P2_1/m$	$Pm\bar{3}m$ at 186 K; $R3c$ at RT[56,57]	0.90
CsPbCl$_3$	-63.8	-85.5	-85.3		$Pm\bar{3}m$ at 320 K; $Pnma$ at 310 K[15]	0.87
CsPbBr$_3$	-72.5	-100.5	-100.4	$P2_1/m$	$Pm\bar{3}m$ at 403 K ; $Pnma$ at 361 K[58]	0.86
CsPbI$_3$	-94.4	-137.5	-137.3	$Pnma$	$Pm\bar{3}m$ at 634 K[45]	0.85
RbGeF$_3$	-0.7	-0.1	-0.7			1.05
RbGeCl$_3$	-8.2	-1.8	-12.3			0.98
RbGeBr$_3$	-17.8	-22.4	-26.5			0.97
RbGeI$_3$	-41.3	-47.4	-65.2		$Pm\bar{3}m$ at 533 K[47]	0.95
RbSnF$_3$	-73.2	-97.9	-97.9			0.87
RbSnCl$_3$	-105.4	-156	-155.8			0.84
RbSnBr$_3$	-103.7	-158.2	-157.7	$Pnma$ and $P2_1/m$		0.84
RbSnI$_3$	-117.5	-185.9	-185.7	$Pnma$ and $P2_1/m$		0.83
RbPbF$_3$	-134.9	-188.4	-188.3	$Pnma$ and $P2_1/m$	$Pm\bar{3}m$ at 515 K ; $Pnma$ at RT[48]	0.86
RbPbCl$_3$	-170.4	-249.2	-196.7	$Pnma$		0.83
RbPbBr$_3$	-171.3	-255.2	-197.1	$Pnma$ and $P2_1/m$		0.83
RbPbI$_3$	-185.9	-289.4	-289.4	$Pnma$ and $P2_1/m$	$Pm\bar{3}m$ at RT[45]	0.82
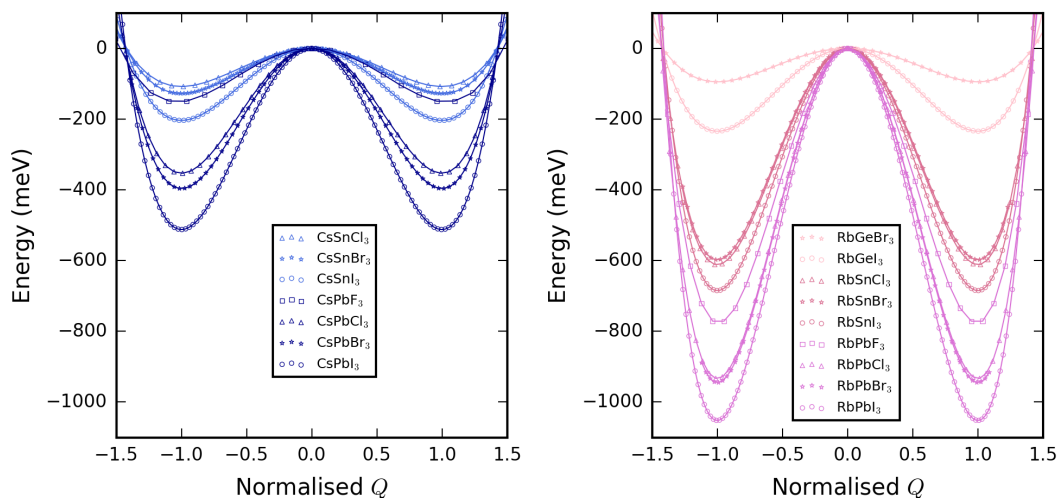
FIG. 2. Double-well potential-energy surfaces for the phonon instabilities associated with M_3^+ tilting modes. The left-hand plot shows data for Cs compounds (lines with blue hue), while the right-hand plot shows data for Rb perovskites (lines with red hue). Halide anions are differentiated by the markers shown in the legends. The normal-mode coordinate Q has been normalised so that for each composition the minima are located at $Q = 1$, and the energy differences are those calculated in a 2×2×2 supercell.

TABLE II. Summary of the imaginary harmonic phonon modes observed for the cubic perovskites. The labels refer to the irreducible representation,[24] and are illustrated in Fig 1b.

Composition	Imaginary Mode			
	Γ	X	M	R
CsGeF$_3$	Γ_4^-	X_5^-	M_2^-	
CsGeCl$_3$	Γ_4^-	X_5^-	M_2^-	
CsGeBr$_3$	Γ_4^-	X_5^-	M_2^-	
CsGeI$_3$	Γ_4^-	X_5^-	M_2^- , M_3^+	R_4^+
CsSnF$_3$	Γ_4^-	X_5^-	M_2^-	R_4^+
CsSnCl$_3$	Γ_4^-		M_3^+	R_4^+
CsSnBr$_3$			M_3^+	R_4^+
CsSnI$_3$	Γ_4^-	X_4^+	M_3^+	R_4^+
CsPbF$_3$	Γ_4^-		M_3^+	R_4^+
CsPbCl$_3$	Γ_4^-	X_4^+	M_3^+	R_4^+
CsPbBr$_3$	Γ_4^-	X_4^+	M_3^+	R_4^+
CsPbI$_3$	Γ_4^-	X_4^+	M_3^+	R_4^+
RbGeF$_3$	Γ_4^-	X_5^-	M_2^- , M_3^+	R_4^+
RbGeCl$_3$	Γ_4^-	X_5^-	M_2^- , M_3^+	R_4^+
RbGeBr$_3$	Γ_4^-	X_5^-	M_3^+	R_4^+
RbGeI$_3$	Γ_4^-	X_5^-	M_3^+	R_4^+
RbSnF$_3$	Γ_4^-	X_5^-	M_2^-	R_4^+
RbSnCl$_3$	Γ_4^-	X_4^+	M_3^+	R_4^+
RbSnBr$_3$	Γ_4^-	X_4^+	M_3^+	R_4^+
RbSnI$_3$	Γ_4^-	X_4^+	M_3^+	R_4^+
RbPbF$_3$	Γ_4^-	X_4^+	M_3^+	R_4^+
RbPbCl$_3$	Γ_4^-	X_4^+	M_3^+	R_4^+
RbPbBr$_3$	Γ_4^-	X_4^+	M_3^+	R_4^+
RbPbI$_3$	Γ_4^-	X_4^+	M_3^+	R_4^+

FIG. 4. Zone-boundary Jahn-Teller distortions in CsGeBr$_3$. Shortening and lengthening of the B–X bonds results in an off-centering of the Ge cation. The corresponding phonon modes have M_2^- or X_5^- irreducible representations. The images show a 2×2×1 supercell of the cubic phase in which the two instabilities appear equivalent; the difference is in the movement of atoms in neighbouring supercells in the out-of-plane direction, which is out of phase in the M_2^- mode but in phase in the X_5^- mode.

electron density. These s^2 lone pairs can exhibit a static or dynamic structural distortion.[55] As the binding energy of the ns^2 orbitals increases down the group (i.e. from Ge to Pb), in part due to a relativistic contraction, the stability of the lower oxidation states also increases - the so-called "inert pair" effect.[63] This explains why Jahn-Teller distortions are present in most of the germanium and the tin-fluoride perovskites.

C. Zone-centre cation displacements

With the exception of CsSnBr$_3$, all the perovskites investigated in this work feature Γ-point phonon instabilities corresponding to a polar Γ_4^- mode.5 The long-range nature of the Γ wavevector means that the displacement can induce a macroscopic polarization.[64] In traditional ferroelectric perovskites, this behaviour occurs through off-centering of the B-site cation, for example Ti in BaTiO$_3$ and PbTiO$_3$. In these halide perovskites, both the A-site and B-site cations are susceptible to displacement.

For the Ge-based perovskites CsGeX$_3$ and RbGeX$_3$, this mode involves the off-centring of the Ge cation or movement of the bonded halogens, in agreement with the experimentally-identified polar space group $R3m$ adopted by CsGeCl$_3$, CsGeBr$_3$, and CsGeI$_3$. On the other hand, for Pb-based perovskites, the off-centring is most pronounced at the A site (i.e. Cs or Rb are displaced), while Pb remains at the centre of the octahedron.

For Sn-based compounds, the displacement depends on the halide anions. For CsSnF$_3$, the largest components of the Γ_4^- modes are attributed to F, with minor contributions from Sn and Cs. This is due to the light mass of fluorine. Heavier halogens induce relatively more motion of the A-site and B-site cations.
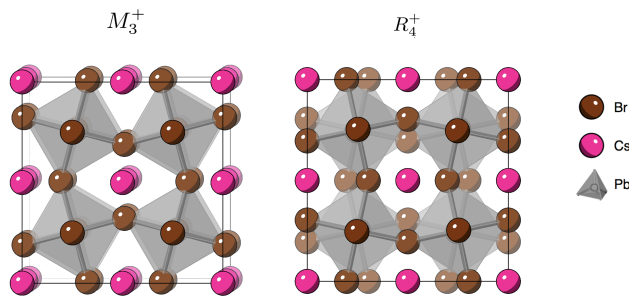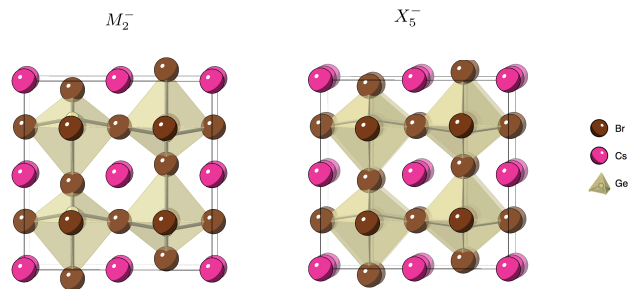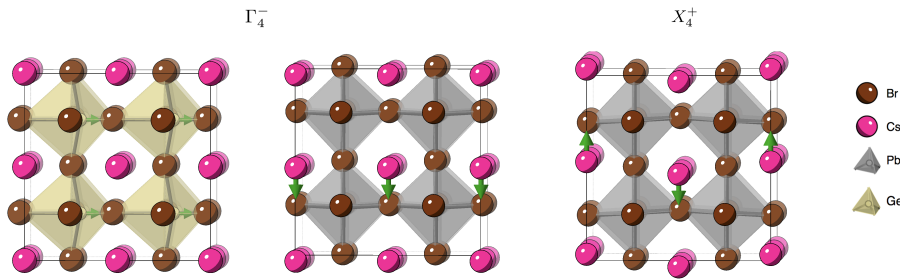

FIG. 3. Distortion of the cubic perovskite structure by condensation of the M_3^+ and R_4^+ tilting modes in CsPbBr$_3$. The M_3^+ and R_4^+ modes correspond to in-phase and out-of-phase tilting in successive layers, respectively.

from the centre of the octahedron.

All of these compounds have large tolerance factors ranging from 0.95 to 1.1, meaning there is limited space for the octahedra to rotate. Instead, the electronic configuration of the B-site cation plays a key role. The electronic configuration ns^2np^0 for heavy group 14 elements (Ge, Sn and Pb) is commonly associated with distorted and non-centrosymmetric coordination environments. The valence p orbitals of the halide mix with the cation s and p orbitals, resulting in a asymmetric

FIG. 5. Change in crystal structure following the Γ_4^- mode in both CsGeBr$_3$ and CsPbBr$_3$ and the X_5^+ mode in CsPbBr$_3$. For CsGeBr$_3$, the Γ_4^- mode corresponds to a B-site displacement, whereas in CsPbBr$_3$ the same mode corresponds to an A-site displacement. For CsPbBr$_3$, the X_5^+ mode also corresponds to an A-site displacement, but with out-of-phase motion in neighbouring unit cells.
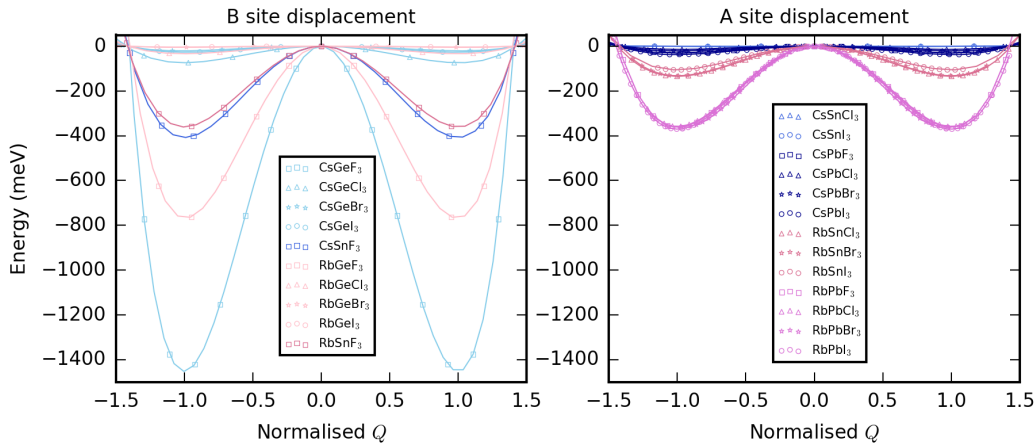

FIG. 6. Comparison of the potential-energy surface in the ABX$_3$ halide perovskites with the polar Γ_4^- instabilities. The Γ_4^- instabilities are categorized into B-site displacement and A-site displacement. Lines with blue hue and red hue corresponds to Cs and Rb compounds, respectively, and the halide anions are indicated by different markers. The normal-mode coordinate Q has been normalised so that the minima of the wells are located at $Q = 1$.

It is worth noting that the Γ-point modes involving mostly the Cs or Rb atoms are relatively flat across reciprocal space, characteristic of decorrelated rattling that would not generate macroscopic polarization. This explains why Pb and Sn-based perovskites have not been identified in polar space groups.

The X-mode instabilities also involve cation displacement. The X_4^+ distortion involves motion of the A-site cation (5), whereas the X_5^- mode leads to displacement of the B-site cation. Similar chemical trends as observed for the Γ-point instabilities can also be seen in the X modes. CsGeX$_3$, RbGeX$_3$, CsSnF$_3$ and RbSnF$_3$ show X_5^- instabilities that result in B-site off centring, whereas the other Sn-based and all the Pb-based perovskites undergo X_4^+ distortions leading to A site displacement. The key difference between X- and Γ-point phonon instabilities is that the former involves out-of-phase displacement in neighbouring unit cells along one real-space direction.

To compare the energy landscape associated with the different cation displacements, we mapped out the potential energy surfaces for representative Γ_4^- modes (Fig.6).

For the A-site displacement, it is obvious that the double well is deeper for Rb compounds than Cs compounds (e.g. CsPbX$_3$ vs. RbPbX$_3$), which can be explained by the relatively small ionic radius of Rb (1.72 Å, tolerance factor: 0.82–0.86 for RbPbX$_3$). In both the Cs and Rb series, changing the B-site cation from Sn to Pb results in a deeper double well potential.

On the other hand, the difference between Cs and Rb compounds is not as large for B-site displacement but depends much more strongly on the halide. For the CsGeX$_3$ and RbGeX$_3$ series (X = Cl, Br, I), and for CsGeF$_3$, RbGeF$_3$, CsSnF$_3$ and RbSnF$_3$, the B-site instabilities are associated with deep energetic minima. For the latter four compounds, the Γ_4^- instabilities are accompanied by large distortions to the cage, which results in a correspondingly large reduction in energy. This is consistent with the fact that none of these systems have been experimentally identified. The trend in the B-site displacement indicates that the displacement of the B-site cation within the octahedra is largely independent of the A-site cation, but is affected by the bonding environment

within the octahedra.

Except for the anomalous fluoride compounds, the energy minima associated with cation displacement are much shallower than those for octahedral tilting, suggesting it to be a secondary effect in reducing the energy.

VI. DISCUSSION AND CONCLUSIONS

From a bonding perspective, a larger tolerance factor α implies that A-site cation sits in a relatively tight bonding environment and the octahedral network is less prone to tilting. This is evident when the potential-energy minima along the tilt modes are plotted against tolerance factor (Fig. 7). As α approaches unity, the well depths associated with the tilting modes (M_3^+ and R_4^+) become shallower, suggesting weaker tilting instabilities. There is no obvious difference between M_3^+ and R_4^+ modes, implying that in-phase and out-of-phase tilting are similarly favoured energetically.

Such trends, however, are not present for the zone-boundary Jahn-Teller distortion (Fig. 7), suggesting that they are not a product of the geometry alone. The distortions occur in compound with $\alpha >$ than 0.9, whereas the tilting mode is more pronounced for compounds with $\alpha < 0.9$. This indicates that the JT mode is favoured in relatively small octahedra, which is usually associated with smaller B-site cations and halogen atoms. Also, our calculations show little energetic difference between M_2^- and X_5^- modes, the two JT-related instabilities.

For cation displacement, there is a distinction between A- and B-site behavior. A clear boundary could be drawn at $\alpha \approx 0.9$, below which A-site displacement is energetically favoured and above which off-centring of the B-site cation is favoured. While both are driven by the same JT distortions, A-site displacement can only be accommodated when the cuboctahedral cavity is large enough, which explains the relation to the tolerance factor. The energy gain (well depths) for cation displacements are generally much smaller than the for other two types of distortions.

At high temperature, these perovskites fluctuate between equivalent structural minima. The depth of the well and the temperature determine the classical hopping rate between two local minima through the Arrhenius equation $\Gamma = \nu\exp(-\Delta E/k_B T)$, where ν is the attempt frequency.[29] At high temperature, the compositions with small energy barriers have fast hopping rates and display dynamic disorder, which leads to a cubic symmetry in diffraction on average. On the other hand, those with larger energy barriers show static disorder with slow hopping rates.

Deeper wells lead to a higher phase transition temperature to the cubic phase. This is confirmed by the correlation between the calculated well depths and the measured phase transition temperature (Table I). Although it is not possible to predict the precise phase transition temperature with the single-mode potential sur-

faces – this would require high-order anharmonic phonon calculations – it provides a qualitative trend. The distortion modes identified in the high-temperature cubic phase start to condense when the temperature decreases, i.e. the structures start to follow the distortion vectors to lower the energy of the system. For example, the tetragonal phase results from the M_3^+ in-phase tilting mode, whereas the orthorhombic $Pnma$ phase results from a combination of M_3^+ and R_4^+ out-of-phase tilting modes.[24]

We note that all compositions have these phonon modes, and that the modes are highly anharmonic – they coexist in perovskite crystals and may couple with each other. Here we have treated each mode independently while "locking in" the other modes. The interaction of different modes requires an explicit treatment of anharmonicity[65,66] or large-scale molecular dynamics simulations, which is an interesting direction for future research.

In conclusion, we have carried out a systematic study of the phonon instabilities in inorganic halide perovskites. By explicitly mapping the potential-energy surfaces associated with the three classes of instability, we have quantified the relation between the structure and chemistry and the dominant phonon instabilities. All cubic perovskites show octahedral-tilting instabilities, but the magnitude of the tilting and the associated energetic gains depend on the interplay of the A-site cation and the octahedral cage. The JT distortion and B-site displacement both tend to occur in Ge and fluorine compounds due to s/p orbital interactions. A-site cation displacement is favoured when the cation is much smaller than the cage, but results in a moderate energy gain compared to other instabilities. Amongst all instabilities, the octahedral tilting is energetically the most dominant instability. Therefore, our categorization and quantification of the instabilities is especially important in directing the synthesis of new functional inorganic halide perovskites.
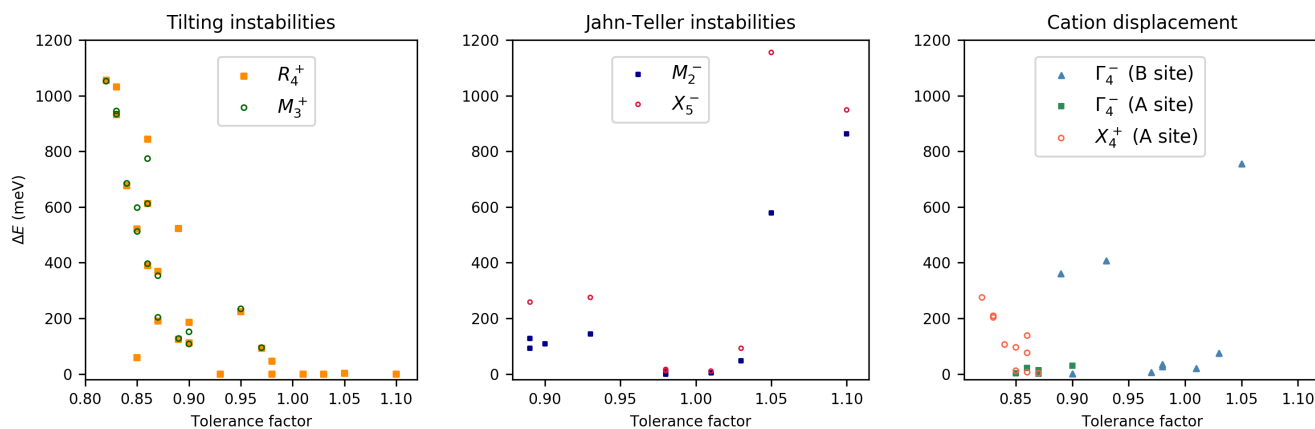
FIG. 7. Relationship between geometric tolerance factor α and well depths associated with different types of phonon instabilities. The tilting instability decreases as tolerance factor increases, while the other two types of instability depend more on the chemistry rather than geometric constraints.

[1] C. K. Møller, Nature **182**, 1436 (1958).

[2] J. D. Donaldson, J. Silver, S. Hadjiminolis, and S. D. Ross, J. Chem. Soc., Dalton Trans. **1975**, 1500 (1975).

[3] U. Schwarz, H. Hillebrecht, M. Kaupp, K. Syassen, H.-G. von Schnering, and G. Thiele, J. Solid State Chem. **118**, 20 (1995).

[4] G. Thiele, H. W. Rotter, and K. D. Schmidt, Zeitschrift für Anorg. und Allg. Chemie **545**, 148 (1987).

[5] D. B. Mitzi, C. A. Feild, W. T. A. Harrison, and A. M. Guloy, Nature **369**, 467 (1994).

[6] A. Kojima, K. Teshima, Y. Shirai, and T. Miyasaka, J. Am. Chem. Soc. **131**, 6050 (2009).

[7] M. M. Lee, J. Teuscher, T. Miyasaka, T. N. Murakami, and H. J. Snaith, Science **338**, 643 (2012).

[8] Z. Ning, X. Gong, R. Comin, G. Walters, F. Fan, O. Voznyy, E. Yassitepe, A. Buin, S. Hoogland, and E. H. Sargent, Nature **523**, 324 (2015).

[9] C. S. Ponseca, T. J. Savenije, M. a. Abdellah, K. Zheng, A. P. Yartsev, T. Pascher, T. Harlang, P. Chabera, T. Pullerits, A. Stepanov, J.-p. Wolf, and V. Sundstrom, J. Am. Chem. Soc. **136**, 5189 (2014).

[10] C. Wehrenfennig, G. E. Eperon, M. B. Johnston, H. J. Snaith, and L. M. Herz, Adv. Mater. **26**, 1584 (2014).

[11] Y. Yuan, J. Chae, Y. Shao, Q. Wang, Z. Xiao, A. Centrone, and J. Huang, Adv. Energy. Mater. **5**, 1500615 (2015).

[12] S. D. Stranks, G. E. Eperon, G. Grancini, C. Menelaou, M. J. P. Alcocer, T. Leijtens, L. M. Herz, A. Petrozza, and H. J. Snaith, Science **342**, 341 (2013).

[13] M. Shirayama, H. Kadowaki, T. Miyadera, T. Sugita, M. Tamakoshi, M. Kato, T. Fujiseki, D. Murata, S. Hara, T. N. Murakami, S. Fujimoto, M. Chikamatsu, and H. Fujiwara, Phys. Rev. Applied **5**, 014012 (2016).

[14] D. Weber, Zeitschrift für Naturforsch. **33b**, 1443 (1978).

[15] Y. Fujii, S. Hoshino, Y. Yamada, and G. Shirane, Phys. Rev. B **9**, 4549 (1974).

[16] R. J. Worhatch, H. J. Kim, I. P. Swainson, A. L. Yonkeu, and S. J. L. Billinge, Chem. Mater. **20**, 1272 (2008).

[17] A. N. Beecher, O. E. Semonin, J. M. Skelton, J. M. Frost, M. W. Terban, H. Zhai, A. Alatas, J. S. Owen, A. Walsh, and S. J. L. Billinge, ACS Energy Lett. **1**, 880 (2016).

[18] R. Comin, M. K. Crawford, A. H. Said, N. Herron, W. E. Guise, X. Wang, P. S. Whitfield, A. Jain, X. Gong, A. J. H. McGaughey, and E. H. Sargent, Phys. Rev. B **94**, 094301 (2016).

[19] K. Page, J. E. Siewenie, P. Quadrelli, and L. Malavasi, Angew. Chemie - Int. Ed. **55**, 14320 (2016).

[20] F. Bertolotti, L. Protesescu, M. V. Kovalenko, S. Yakunin, A. Cervellino, S. J. L. Billinge, M. W. Terban, J. S. Pedersen, N. Masciocchi, and A. Guagliardi, ACS Nano **11**, 3819 (2017).

[21] O. Yaffe, Y. Guo, L. Z. Tan, D. A. Egger, T. Hull, C. C. Stoumpos, F. Zheng, T. F. Heinz, L. Kronik, M. G. Kanatzidis, J. S. Owen, A. M. Rappe, M. A. Pimenta, and L. E. Brus, Phys. Rev. Lett. **118**, 136001 (2017).

[22] J. A. Steele, P. Puech, B. Monserrat, B. Wu, R. X. Yang, T. Kirchartz, H. Yuan, G. Fleury, D. Giovanni, E. Fron, M. Keshavarz, E. Debroye, G. Zhou, T. C. Sum, A. Walsh, J. Hofkens, and M. B. J. Roeffaers, ACS Energy Lett. **4**, 2205 (2019), https://doi.org/10.1021/acsenergylett.9b01427.

[23] P. M. Woodward, Acta Crystallogr. Sect. B Struct. Sci. **53**, 32 (1997).

[24] C. J. Howard and H. T. Stokes, Acta Crystallogr. Sect. B **54**, 782 (1998).

[25] N. A. Benedek and C. J. Fennie, J. Phys. Chem. C **117**, 13339 (2013).

[26] J. B. Neaton, C. Ederer, U. V. Waghmare, N. A. Spaldin, and K. M. Rabe, Phys. Rev. B **71**, 014113 (2005).

[27] W. J. Merz, Phys. Rev. **76**, 1221 (1949).

[28] A. M. Glazer, Acta Crystallogr. Sect. B Struct. Crystallogr. Cryst. Chem. **28**, 3384 (1972).

[29] R. X. Yang, J. M. Skelton, E. L. Da Silva, J. M. Frost, and A. Walsh, J. Phys. Chem. Lett. **8**, 4720 (2017).

[30] J. K. Burdett, Inorg. Chem. **20**, 1959 (1981).

[31] N. A. Benedek and C. J. Fennie, Phys. Rev. Lett. **106**, 107204 (2011).

[32] J. Young, A. Stroppa, S. Picozzi, and J. Rondinelli, J. Phys. Condens. Matter **27**, 283202 (2015).

[33] J. Varignon, N. C. Bristowe, E. Bousquet, and P. Ghosez, Sci. Rep. **5**, 15364 (2015).

[34] N. C. Bristowe, J. Varignon, D. Fontaine, E. Bousquet, and P. Ghosez, Nat. Commun. **6**, 6677 (2015).

[35] G. Kresse and J. Furthmüller, Phys. Rev. B **54**, 11169 (1996).

[36] G. Kresse and J. Furthmüller, Comput. Mater. Sci. **6**, 15 (1996).

[37] J. P. Perdew, A. Ruzsinszky, G. I. Csonka, O. A. Vydrov, G. E. Scuseria, L. A. Constantin, X. Zhou, and K. Burke, Phys. Rev. Lett. **100**, 136406 (2008).

[38] J. P. Perdew, A. Ruzsinszky, G. I. Csonka, O. A. Vydrov, G. E. Scuseria, L. A. Constantin, X. Zhou, and K. Burke, Phys. Rev. Lett. **102**, 39902 (2009), arXiv:0711.0156v3.

[39] G. Bergerhoff, R. Hundt, R. Sievers, and I. D. Brown, J. Chem. Inf. Comput. Sci. **23**, 66 (1983).

[40] J. M. Skelton, L. A. Burton, S. C. Parker, A. Walsh, C.-E. Kim, A. Soon, J. Buckeridge, A. A. Sokol, C. R. A. Catlow, A. Togo, and I. Tanaka, Phys. Rev. Lett. **117**, 075502 (2016).

[41] J. M. Skelton, "ModeMap," https://github.com/JMSkelton/ModeMap.

[42] A. N. Christensen and S. E. Rasmussen, ACTA Chem. Scand. **19**, 421 (1965).

[43] M. Ahtee, K. Kurki-Suonio, A. Vahvaselkä, A. W. Hewat, J. Harada, and S. Hirotsu, Acta Crystallogr. Sect. B **36**, 1023 (1980).

[44] M. Sakata, N. Takash, and H. Jimpei, J. Phys. Soc. Japan **47**, 232 (1979).

[45] D. Trots and S. Myagkota, J. Phys. Chem. Solids **69**, 2520 (2008).

[46] I. Chung, J. H. Song, J. Im, J. Androulakis, C. D. Malliakas, H. Li, A. J. Freeman, J. T. Kenney, and M. G. Kanatzidis, J. Am. Chem. Soc. **134**, 8579 (2012).

[47] G. Thiele, H. W. Rotter, and K. D. Schmidt, Z. Anorg. Allg. Chem. **571**, 60 (1989).

[48] Y. Yamane, K. Yamada, and K. Inoue, Solid State Ionics **179**, 605 (2008).

[49] V. M. Goldschmidt, Naturwissenschaften **14**, 477 (1926).

[50] D.-K. Seo, N. Gupta, M.-H. Whangbo, H. Hillebrecht, and G. Thiele, Inorg. Chem. **37**, 407 (1998).

[51] R. D. Shannon, Acta Crystallogr. Sect. A **32**, 751 (1976).

[52] G. Kieslich, S. Sun, and T. Cheetham, Chem. Sci. **6**, 3430 (2015).

[53] K. Yamada, K. Isobe, T. Okuda, and Y. Furukawa, Zeitschrift Naturforschung Teil A **49**, 258 (1994).

[54] J. Barrett, S. R. A. Bird, J. D. Donaldson, and J. Silver, J. Chem. Soc. A , 3105 (1971).

[55] D. H. Fabini, G. Laurita, J. S. Bechtel, C. C. Stoumpos, H. A. Evans, A. G. Kontos, Y. S. Raptis, P. Falaras, A. Van der Ven, M. G. Kanatzidis, and R. Seshadri, J. Am. Chem. Soc. **138**, 11820 (2016).

[56] R. Clarke, E. Marseglia, and H. P. Hughes, Philos. Mag. Part B **38**, 121 (1978).

[57] P. Berastegui, S. Hull, and S. Eriksson, J. Phys. Condens. Matter **13**, 5077 (2001).

[58] S. Hirotsu, J. Harada, M. Iizumi, and K. Gesi, J. Phys. Soc. Japan **37**, 1393 (1974).

[59] S. Picozzi, K. Yamauchi, I. A. Sergienko, C. Sen, B. Sanyal, and E. Dagotto, J. Phys. Condens. Matter **20**, 434208 (2008).

[60] G.-J. Yang, B. Ding, Y. Li, S.-Y. Huang, Q.-Q. Chu, C. Li, and C. Li, J. Mater. Chem. A **5**, 6840.

[61] R. D. King-Smith and D. Vanderbilt, Phys. Rev. B **49**, 5828 (1994).

[62] W. Zhong, D. Vanderbilt, and K. M. Rabe, Phys. Rev. B **52**, 6301 (1995).

[63] A. Walsh, D. J. Payne, R. G. Egdell, and G. W. Watson, Chem. Soc. Rev. **40**, 4455 (2011).

[64] H. T. Stokes, E. H. Kisi, D. M. Hatch, and C. J. Howard, Acta Crystallogr. Sect. B **58**, 934 (2002).

[65] N. R. Werthamer, Phys. Rev. B **1**, 572 (1970).

[66] I. Errea, M. Calandra, and F. Mauri, Phys. Rev. B **89**, 064302 (2014).